

UNIVERSIDADE ESTADUAL DE CAMPINAS  
SISTEMA DE BIBLIOTECAS DA UNICAMP  
REPOSITÓRIO DA PRODUÇÃO CIENTÍFICA E INTELLECTUAL DA UNICAMP

**Versão do arquivo anexado / Version of attached file:**

Versão do Editor / Published Version

**Mais informações no site da editora / Further information on publisher's website:**

<https://www.sciencedirect.com/science/article/pii/S0030399222007848>

**DOI: <https://doi.org/10.1016/j.optlastec.2022.108638>**

**Direitos autorais / Publisher's copyright statement:**

©2023 by Elsevier. All rights reserved.

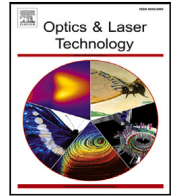
DIRETORIA DE TRATAMENTO DA INFORMAÇÃO

Cidade Universitária Zeferino Vaz Barão Geraldo

CEP 13083-970 – Campinas SP

Fone: (19) 3521-6493

<http://www.repositorio.unicamp.br>



## Full length article

# Novel compact magnetless isolator based on a magneto-optical garnet material

Gianni Portela<sup>a,\*</sup>, Miguel Levy<sup>b</sup>, Hugo E. Hernandez-Figueroa<sup>a</sup><sup>a</sup> School of Electrical and Computer Engineering, University of Campinas, Campinas, 13083-852, SP, Brazil<sup>b</sup> Physics Department, Michigan Technological University, Houghton, MI 49931, USA

## ARTICLE INFO

## Keywords:

Isolators

Optical communication systems

Magneto-optical materials

Temporal coupled-mode theory

## ABSTRACT

A compact magnetless isolator for optical communication systems based on a ring resonator with an outer layer made of silicon and an inner layer made of a magneto-optical material that does not require an external magnet to keep its magnetization saturated is suggested. Three-dimensional computational simulations of the device performed with the full-wave electromagnetic solver COMSOL Multiphysics show that the insertion loss and isolation levels are about  $-1.9$  dB and  $-23$  dB, respectively, thus confirming the feasibility of the isolator. An analytical model of the device based on the temporal coupled-mode theory method has been formulated and there is a good agreement between the analytical and simulation results. Since it does not require a magnetization scheme based on permanent magnets or electromagnets as conventional isolators do, the presented isolator is much more compact, with a footprint at least one order of magnitude smaller in comparison with other isolator designs known from the literature, and this feature makes the suggested device an ideal candidate for optical circuits with very high integration density.

## 1. Introduction

In optical communication systems, the stable operation of signal sources (e.g., LASERS and amplifiers) relies on strategies used to mitigate the harmful effects caused by parasitic reflections arising from unmatched elements. One of the main alternatives for blocking such reflections and avoiding instabilities in the operation of signal sources consists in using optical isolators [1–3]. In this case, one must connect the signal source to the input port of the isolator, while the receiver is connected to the output port of the isolator. Since isolators allow propagation in only one direction, the input power can be transmitted to the receiver, while parasitic reflections are blocked by the isolator.

Most optical isolator designs are based on the utilization of magneto-optical (MO) materials magnetized by external magnets, since such materials enable the nonreciprocal behavior of the device by breaking the time reversal symmetry [4–6]. The static field generated by the external magnet must be strong enough to saturate the magnetization of the material, otherwise the MO activity of the material is drastically reduced and the operation of the isolator is compromised.

One of the challenges for the design of optical communication systems with very high integration density is related to the footprint of the required optical isolators. Permanent magnets and electromagnets used for the magnetization of typical MO materials used in isolator designs are usually very bulky and, as a result, conventional isolators

with external magnets are not suitable when one thinks about optical circuits made of several devices with micrometer or even nanometer dimensions.

For example, the optical isolator suggested in [7] is based on a SOI ring resonator scheme and operates at the 1550 nm wavelength. A MO layer made of cerium-substituted yttrium iron garnet (Ce:YIG) is bonded on the microring structure and a planar spiral electromagnet is used to saturate the magnetization of the MO material. The isolation level of the isolator is better than  $-25$  dB, its operating bandwidth is about 8 GHz and the device footprint is approximately  $3600 \mu\text{m}^2$ .

Another optical isolator design is presented in [8]. This one is also based on the bonding of a Ce:YIG layer on a SOI based structure comprising a ring resonator coupled to a bus waveguide. A gold microstrip coil is used for the magnetization of the MO layer and the footprint of the device is about  $6500 \mu\text{m}^2$ , while the isolation levels and the operating bandwidth near the 1555 nm wavelength are about  $-32$  dB and 1.2 GHz, respectively.

In this work, we present a new optical isolator that is much more compact when compared to conventional isolator designs already referred in the literature because it does not need any bias magnets. In comparison with the isolators presented in [7,8], the footprint of the suggested isolator is one order of magnitude smaller (about  $350 \mu\text{m}^2$ ).

\* Corresponding author.

E-mail address: [masaki@unicamp.br](mailto:masaki@unicamp.br) (G. Portela).<https://doi.org/10.1016/j.optlastec.2022.108638>

Received 4 May 2022; Received in revised form 30 July 2022; Accepted 29 August 2022

Available online 13 September 2022

0030-3992/© 2022 The Author(s). Published by Elsevier Ltd. This is an open access article under the CC BY license (<http://creativecommons.org/licenses/by/4.0/>).

We suggest a device layout for operation around the 1310 nm wavelength as a proof-of-concept demonstration, although one can adapt the layout with a view to operation in other optical wavelengths.

The MO material used in the suggested device is a commercially available bismuth-substituted iron garnet with molecular formula  $\text{Bi}_x(\text{Eu}_z\text{Ho}_{1-z})_{3-x}\text{Fe}_{5-y}\text{Ga}_y\text{O}_{12}$  and it can keep a saturated magnetic state even in the absence of a static magnetic field [9].

A magnetless optical isolator is also suggested in [10]. In this design, a MO layer made of cobalt ferrite (CFO) films is deposited by a sputtering method on top of a silicon racetrack resonator. However, the material losses of CFO films are very high (about 3.4 dB/ $\mu\text{m}$ ) in comparison with those of the MO material used in our design (about 0.0002 dB/ $\mu\text{m}$ ) and, as a consequence, the insertion loss levels of our design (about -1.9 dB) are much better than those of the design presented in [10] (about -11.2 dB).

Additionally, the footprint of the isolator suggested in this paper is one order of magnitude smaller in comparison with the footprint of the isolator presented in [10] (about 3200  $\mu\text{m}^2$ ), that is, the suggested isolator is much more compact and appropriate for photonic circuits with high integration density.

Realistic three-dimensional simulations of the device have been performed with the software product COMSOL Multiphysics, a full-wave electromagnetic solver based on the Finite Element Method (FEM). The numerical results obtained from the simulations evince the feasibility of the proposed magnetless optical isolator.

Besides, we have employed the temporal coupled-mode theory (TCMT) method in order to obtain an analytical model of the device. This model provides a deeper understanding of the device operation in terms of decay rates and resonant frequencies of resonator modes and the analytical results are in good agreement with those acquired from the computational simulations.

## 2. Materials and methods

### 2.1. Isolator design

We have considered a ring resonator structure in a SOI platform for the design of the magnetless isolator. A bus waveguide made of silicon is coupled to a ring resonator comprising an outer layer made of silicon and an inner layer made of a MO material, as schematically shown in Fig. 1.

The width of the bus waveguide is  $w_w = 340$  nm, while the width of the inner and outer layers of the ring resonator are  $w_i = 255$  nm and  $w_o = 405$  nm, respectively. Both the silicon and MO layers have thickness  $h = 185$  nm and there is a gap  $g = 85$  nm between the bus waveguide and the outer layer of the ring resonator.

Regarding the ring resonator, it is a racetrack one with external bend radius  $R = 3.8$   $\mu\text{m}$  and straight section length  $L = 30.5$   $\mu\text{m}$ . The racetrack ring resonator also includes a slightly convex section defined by the parameters  $L_c = 7.8$   $\mu\text{m}$  and  $c = 1.2$   $\mu\text{m}$ .

The device operates with Transverse Electric (TE) waveguide modes and we have considered, in our computational simulations, that the refractive indexes of silicon (Si) and silica ( $\text{SiO}_2$ ) are  $n_{\text{Si}} = 3.5$  and  $n_{\text{SiO}_2} = 1.45$ , respectively [11,12].

The suggested device layout is a proof-of-concept demonstration at the specific 1310 nm wavelength. For operation at other optical wavelengths (e.g., 1550 nm), one can resize the entire layout or one can take advantage of wavelength conversion techniques, such as those based on four-wave mixing (FWM) suggested in [13,14].

### 2.2. Properties of the magneto-optical material

The inner layer of the racetrack ring resonator is made of a MO garnet material with molecular formula  $\text{Bi}_x(\text{Eu}_z\text{Ho}_{1-z})_{3-x}\text{Fe}_{5-y}\text{Ga}_y\text{O}_{12}$ . The magnetless operation of the suggested isolator is feasible because this MO material does not require any external magnets in order to keep its magnetization saturated.

More specifically, the amount of europium (Eu) is maximized in the material and, as a result, its saturation magnetization is reduced (between 10 G and 60 G), without the creation of a compensation point [9,15]. In the formula unit of the material, the parameters  $X$ ,  $Y$ , and  $Z$  are the bismuth concentration, gallium concentration, and the europium fraction of rare earth in the film, respectively. In our calculations, we have considered  $X = 1.22$ ,  $Y = 0.956$ , and  $Z = 0.45$ . Besides, we have neglected in our simulations the effect of MO material losses because the loss per micron of the material is very small (about 0.0002 dB) [16].

We have opted for a proof-of-concept demonstration of the device at the 1310 nm wavelength, instead of at the more typical 1550 nm wavelength, because the specific Faraday rotation coefficient  $\theta_F$  of the MO material is larger at the 1310 nm wavelength than at the 1550 nm wavelength [16].

The refractive index and the specific Faraday rotation coefficient of the MO material, at the 1310 nm wavelength, are  $n_{\text{MO}} = 2.327$  and  $\theta_F = 1410$  deg/cm, respectively [15,16]. The permittivity tensor of the material can be defined as follows:

$$[\epsilon] = \epsilon_0 \begin{pmatrix} \epsilon_r & -i\epsilon_a & 0 \\ i\epsilon_a & \epsilon_r & 0 \\ 0 & 0 & \epsilon_r \end{pmatrix}, \quad (1)$$

where  $\epsilon_r = n_{\text{MO}}^2$  and the off-diagonal element  $\epsilon_a$  is about 0.0024.

### 2.3. Fabrication aspects

The fabrication of the device mainly consists of patterning the silicon elements and bonding of the MO material on the SOI structure. The silicon bus waveguide and ring resonator outer layer can be patterned by using conventional methods like plasma-enhanced chemical vapor deposition (P-CVD), electron-beam (EB) lithography and reactive ion etching (RIE). The utilization of such methods on the patterning of SOI structures is described in [10].

Regarding the bonding of the MO material on the SOI substrate, the direct wafer bonding technique suggested in [7,17,18] is one of the alternatives. The main challenge concerning the utilization of this technique is the creation of a gap between the sidewalls of the silicon and MO layers of the resonator. This gap can lead to performance degradation and some adaptations in the technique would be required in order to reduce such gap.

## 3. Theoretical analysis of the device

### 3.1. Scattering matrix analysis

The antiplane of symmetry  $T\sigma$  shown in Fig. 2 is an element of the symmetry group of the isolator. From the commutation relation  $R_{T\sigma}S = S^T R_{T\sigma}$ , where  $R_{T\sigma}$  is the representation matrix of the anti-unitary element  $T\sigma$  and  $S$  is the scattering matrix of the isolator, one can define the following relation regarding the entries of  $S$  [19]:

$$S_{11} = S_{22}. \quad (2)$$

Therefore, one cannot derive a relation regarding the off-diagonal elements  $S_{21}$  and  $S_{12}$  of the scattering matrix  $S$  from the symmetry analysis of the device. In general, one have  $S_{21} \neq S_{12}$ , as one could expect from a nonreciprocal device.

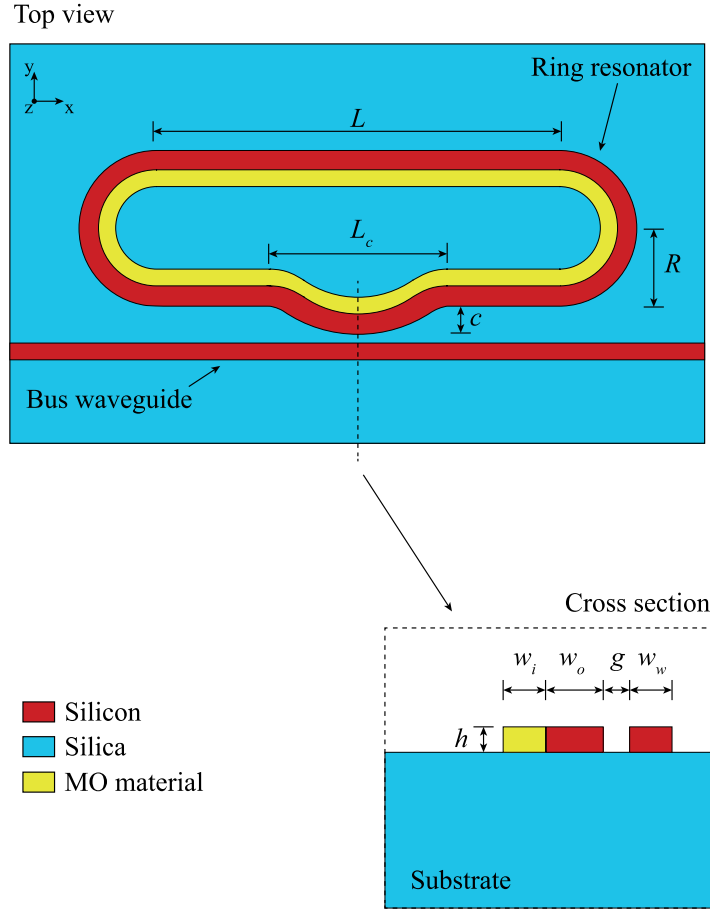
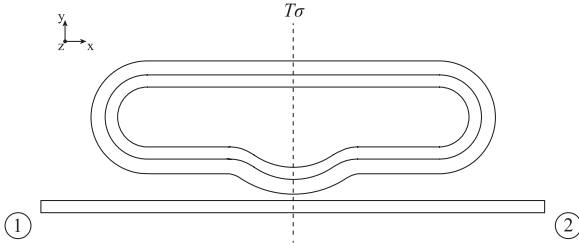


Fig. 1. Schematic view of the isolator.

Fig. 2. Antiplane of symmetry  $T\sigma$ .

Particularly, an input signal coming from port 1 couples to the counterclockwise rotating mode of the resonator, while an input signal coming from port 2 couples to the clockwise rotating mode of the resonator. Since there is a frequency splitting between both modes related to the MO activity of the iron garnet, the resonance peaks of the curves of  $S_{21}$  and  $S_{12}$  take place in different frequencies and  $S_{21} \neq S_{12}$  holds.

### 3.2. Temporal coupled-mode theory method

It is possible to derive formulas for the calculation of the entries of  $S$  from the analytical temporal coupled-mode theory (TCMT) method [20, 21]. It can be used for modeling a set of coupled individual elements, like resonators and waveguides, and its main assumption is the weak coupling between the various elements. The TCMT method is typically considered in the case of reciprocal devices, however, it can be used even in the case of nonreciprocal components, like circulators and isolators [22,23].

By using the methodology described in [22] for nonreciprocal devices, one can derive the following equations for the calculation of the entries of  $S$ -matrix:

$$S_{21}(\omega) = 1 - \frac{\gamma_+}{j(\omega - \omega_+) + \gamma_+ + \gamma_{i+}}, \quad (3)$$

$$S_{12}(\omega) = 1 - \frac{\gamma_-}{j(\omega - \omega_-) + \gamma_- + \gamma_{i-}}, \quad (4)$$

$$S_{11}(\omega) = S_{22}(\omega) = 0. \quad (5)$$

In (3)–(5), the parameters  $\omega_+$ ,  $\gamma_+$ , and  $\gamma_{i+}$  are the resonant frequency, the decay rate due to waveguide coupling, and the decay rate due to intrinsic losses of the counterclockwise rotating mode. Analogously, the TCMT parameters with the subindex “-” refer to the clockwise rotating mode.

In Section 4, we show that the results obtained from the TCMT equations can be quite close to those obtained from the computational simulations of the isolator. Besides, it is possible to obtain a better understanding of the device by studying the influence of each TCMT parameter (decay rates and resonant frequencies) on the curves of  $S$ -parameters generated by (3)–(5).

### 3.3. Frequency response evaluation based on TCMT equations

Let us consider the illustrative frequency response of the isolator shown in Fig. 3. Since we are not interested on the real values of  $S$ -parameters and frequencies at this moment, we show in this figure only typical curves of the  $S_{21}$  and  $S_{12}$  parameters, as well as some reference points that define the operating frequency band of the isolator.

In Fig. 3,  $\Delta\omega_-$  is the bandwidth related to the first resonance defined at the  $n_-$  reference level, with  $\omega_{1-}$  and  $\omega_{2-}$  defining the lower and

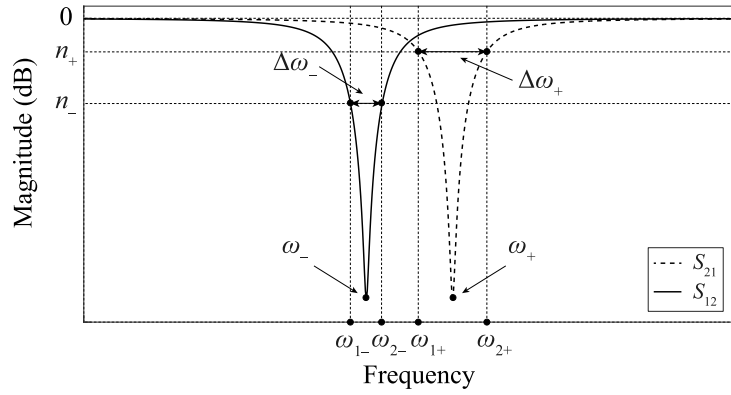


Fig. 3. Illustrative frequency response of the isolator.

upper limits of the corresponding frequency band. Analogously, the parameters with subindex “+” refer to the second resonance of the device.

From (3)–(5), one can derive the following formulas for the parameters shown in Fig. 3:

$$\omega_{1\pm} = \omega_{\pm} - \sqrt{\frac{10^{0.1n_{\pm}} (\gamma_{\pm} + \gamma_{i\pm})^2 - \gamma_{i\pm}^2}{1 - 10^{0.1n_{\pm}}}}, \quad (6)$$

$$\omega_{2\pm} = \omega_{\pm} + \sqrt{\frac{10^{0.1n_{\pm}} (\gamma_{\pm} + \gamma_{i\pm})^2 - \gamma_{i\pm}^2}{1 - 10^{0.1n_{\pm}}}}, \quad (7)$$

$$\Delta\omega_{\pm} = \omega_{2\pm} - \omega_{1\pm} = 2\sqrt{\frac{10^{0.1n_{\pm}} (\gamma_{\pm} + \gamma_{i\pm})^2 - \gamma_{i\pm}^2}{1 - 10^{0.1n_{\pm}}}}. \quad (8)$$

The main difference between the two counter-rotating modes is related to their rotation direction. Since their mode numbers are the same (integer number of wavelengths that fit inside the ring resonator) and the frequency splitting of both modes is relatively small, one can consider, as a good approximation, that the decay rates of both modes are equal, that is,  $\gamma_+ = \gamma_- = \gamma$  and  $\gamma_{i+} = \gamma_{i-} = \gamma_i$ .

Specifically, we will focus on the operation of the isolator around the first resonance (resonance peak of the  $S_{12}$  parameter), since a similar analysis can be performed considering the operation around the second resonance. In this case, the parameters  $n_-$  and  $n_+$  correspond to the isolation and insertion loss levels considered for the calculation of the isolator bandwidth.

One can notice from Fig. 3 that the operating bandwidth of the isolator corresponds to the intersection of the frequency band with bandwidth  $\Delta\omega_-$  and the one corresponding to the interval  $\omega \leq \omega_{1+}$ . Considering, for illustrative purposes, that  $n_- = -10$  dB and  $n_+ = -3$  dB, the following conditions must be met:

1. There must be two real frequencies  $\omega_{1-}$  and  $\omega_{2-}$  for which  $S_{12} = -10$  dB or, equivalently,  $\Delta\omega_-$  must be real and greater than zero.
2.  $\omega_{1+} > \omega_{1-}$ .

If at least one of the above conditions is not met, one cannot ensure, simultaneously, isolation levels better than  $-10$  dB and insertion losses better than  $-3$  dB in a frequency band near the first resonance of the structure. We show in Section 4 that both conditions are satisfied in our design and it is possible to see how to meet them from the TCMT equations.

Regarding the first condition, one can show from (8) that it is satisfied if the following relationship between  $\gamma$  and  $\gamma_i$  remains valid:

$$\gamma > 2.162\gamma_i. \quad (9)$$

This relationship tells us that the decay rate of the resonator mode due to waveguide coupling must be at least 2.162 times greater than

the decay rate of the mode due to intrinsic losses. One can increase the value of  $\gamma$  by tuning the gap  $g$  between the bus waveguide and the resonator, as well as by modifying the shape of the bus waveguide or ring resonator in the region wherein the waveguide–resonator coupling takes place (see [22] for more details). On the other hand, one can decrease the value of  $\gamma_i$  by making use of low-loss materials in the design.

Regarding the second condition, one can show from (6) and (7) that, if the following relationship between the resonant frequencies and the decay rates of the modes is satisfied, then the condition is met:

$$\omega_+ - \omega_- > \sqrt{\gamma^2 + 2\gamma\gamma_i - \gamma_i^2} - \frac{1}{3}\sqrt{\gamma^2 + 2\gamma\gamma_i - 9\gamma_i^2}. \quad (10)$$

The left-hand side of (10) represents the frequency splitting of the counter-rotating modes of the ring resonator and it must be greater than the expression involving the decay rates of the modes in the right-hand side of (10). Equivalently, this relationship shows that the overlap between the counter-rotating modes of the resonator must be decreased with a view to the proper functioning of the isolator.

The simplest method for increasing the value of the left-hand side of (10) consists in using MO materials with high specific Faraday rotation coefficient, while the value of the right-hand side of (10) can be decreased by making the coupling between the resonator modes and the bus waveguide lower. However, one cannot excessively decrease the waveguide coupling  $\gamma$ , otherwise the relationship presented in (9) is not satisfied.

#### 4. Results and discussion

Computational simulations of the suggested magnetless optical isolator have been performed with the full-wave electromagnetic solver COMSOL Multiphysics. We have also calculated the  $S$ -parameters of the device by using the TCMT equations and compared the results obtained from such equations with those acquired from the computational simulations of the device. In the following, we present and discuss the results obtained both from computational simulations and TCMT equations.

##### 4.1. Numerical results obtained from computational simulations

Three-dimensional simulations of the device have been performed with the software product COMSOL Multiphysics. In order to reduce memory consumption and computation time of our simulations, we have inserted a hole in the center of the ring resonator. The center hole and the resonator have the same shape and there is a gap equal to 500 nm between them, so that the electromagnetic fields are negligible in the volume corresponding to the hole and do not need to be calculated.

The  $S$ -parameters of the magnetless isolator for operation around the 1310 nm wavelength are shown in Fig. 4.

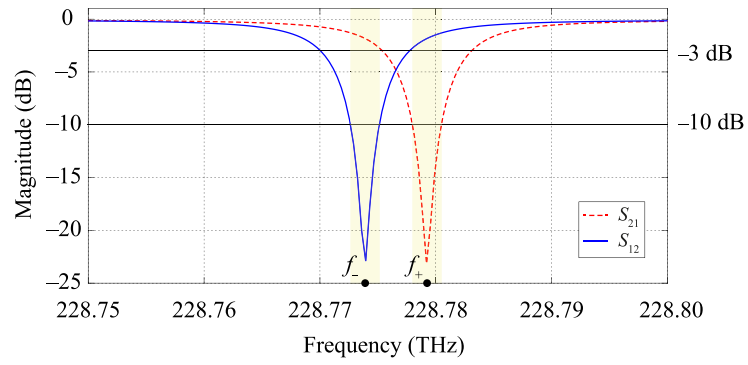


Fig. 4.  $S$ -parameters of the isolator.

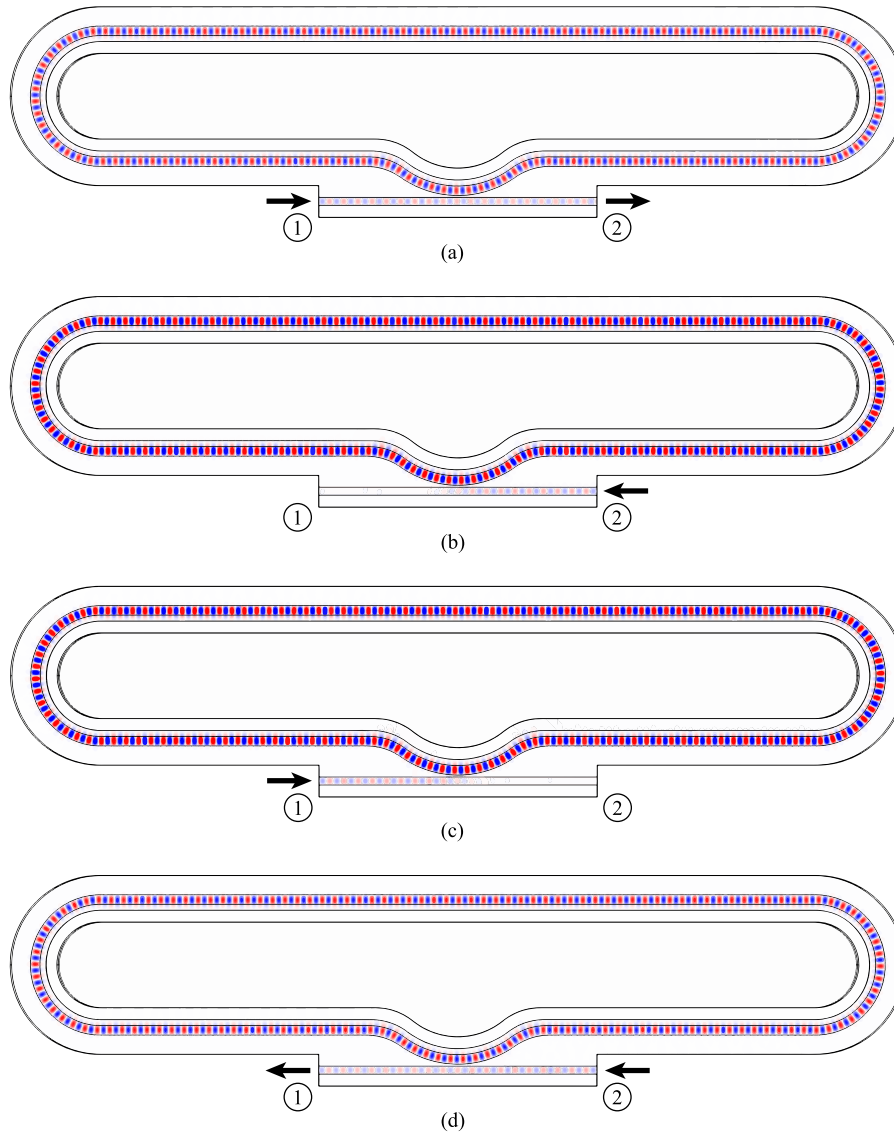


Fig. 5.  $H_z$  field profile in the isolator for (a) input signal applied to port 1 ( $f = f_-$ ), (b) input signal applied to port 2 ( $f = f_-$ ), (c) input signal applied to port 1 ( $f = f_+$ ), and (d) input signal applied to port 2 ( $f = f_+$ ).



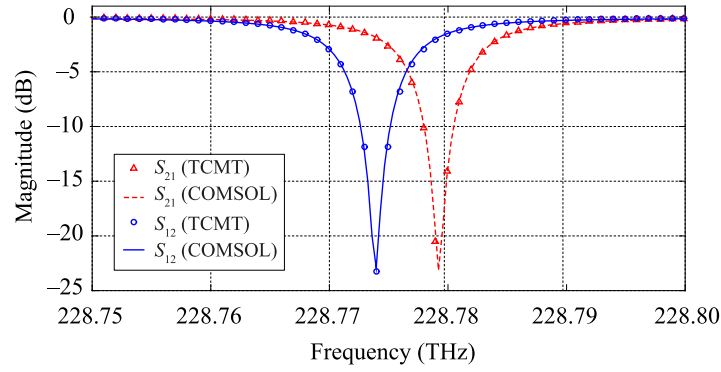


Fig. 6.  $S$ -parameters of the isolator obtained from computational simulations and TCMT equations.

The device has two operating frequency bands, both highlighted in yellow in Fig. 4: one around the first resonance of the ring resonator (with center frequency  $f_-$ ) and the other one around the second resonance of the ring resonator (with center frequency  $f_+$ ).

The bandwidth of the device for operation around the first resonance, defined at the levels  $-3$  dB of the  $S_{21}$  curve and  $-10$  dB of the  $S_{12}$  curve, is 2.51 GHz and, at the center frequency  $f_- = 228.7739$  THz, the insertion loss and isolation levels are about  $-1.8$  dB and  $-22.9$  dB, respectively.

Concerning the operation around the second resonance, the bandwidth of the device is also 2.51 GHz when one considers the  $-3$  dB and  $-10$  dB levels of the  $S_{12}$  and  $S_{21}$  curves, respectively. At the center frequency  $f_+ = 228.7792$  THz, the insertion loss is about  $-1.9$  dB, while the isolation level is about  $-23.1$  dB.

The field profiles of the  $H_z$  component at the center frequencies  $f_-$  and  $f_+$ , considering the input signal applied to ports 1 and 2, are shown in Fig. 5.

One can see from Fig. 5(a) and 5(b) that, at the center frequency  $f_-$ , an input signal applied to port 1 is transmitted to port 2 with low insertion losses, while an input signal applied to port 2 strongly couples to the clockwise rotating mode of the ring resonator and does not reach port 1. On the other hand, one can see from Fig. 5(c) and 5(d) that, at the center frequency  $f_+$ , the opposite situation takes place, that is, an input signal applied to port 1 does not reach port 2 because it strongly couples to the counterclockwise rotating mode of the resonator, while an input signal applied to port 2 is transmitted to port 1 with low insertion losses.

#### 4.2. Analytical results provided by the TCMT method

We have calculated the frequency response of the circulator by using the TCMT equations presented in Section 3.2, in order to show that the presented TCMT-based model of the isolator can be used to evaluate the performance of the device. Fig. 6 presents the  $S$ -parameters obtained from (3) and (4), as well as those acquired from the computational simulations of the device.

There is a good agreement between the results provided by the TCMT equations and those obtained from the 3D simulations of the device performed with COMSOL Multiphysics, as one can see from Fig. 6. We have considered the following values of the TCMT parameters in order to obtain the TCMT curves presented in Fig. 6:  $\gamma_+ = \gamma_- = \gamma = 2.3 \times 10^{10}$  rad/s,  $\gamma_{i+} = \gamma_{i-} = \gamma_i = 0.17 \times 10^{10}$  rad/s,  $\omega_- = 1.437429 \times 10^{15}$  rad/s, and  $\omega_+ = 1.437462 \times 10^{15}$  rad/s.

We have presented in Section 3.3 the two conditions that must be satisfied by the design with a view to obtaining insertion loss and isolation levels better than  $-3$  dB and  $-10$  dB, respectively, in a given frequency band. In order to meet such conditions, we have derived the relationships (9) and (10), which in turn contain the TCMT parameters of the model. One can see that both relationships are satisfied for the aforementioned values of the TCMT parameters.

Specifically, we have  $\gamma \approx 13.5\gamma_i$ , that is, the inequality (9) is satisfied. Besides, the inequality (10) is satisfied, since the left-hand side of (10) is equal to  $3.29 \times 10^{10}$  rad/s and the right-hand side of (10) is equal to  $1.65 \times 10^{10}$  rad/s. We have managed to satisfy these two relationships by properly tuning the geometrical parameters of the design and by making use of low-loss materials, as discussed in Section 3.3.

#### 5. Conclusions

The numerical results presented in this paper, obtained from three-dimensional electromagnetic simulations performed with the software product COMSOL Multiphysics, confirm the feasibility of the suggested magnetless optical isolator.

The elimination of the bias magnet allowed us to reduce the footprint of the design by one order of magnitude in comparison with the designs presented in [7,8,10]. The reduced dimensions of our design make it very appropriate for optical communication systems with high integration density.

Besides, we have employed the TCMT method in order to obtain an analytical model of the device. We have derived formulas for the calculation of the  $S$ -parameters of the isolator and the results obtained from such formulas are in good agreement with those obtained from the 3D simulations of the device. The suggested TCMT-based model allowed us to define relationships concerning the decay rates and resonant frequencies of the resonator modes that must be satisfied and the corresponding discussion can be very useful for the design of similar nonreciprocal devices.

#### CRediT authorship contribution statement

**Gianni Portela:** Conceptualization, Methodology, Validation, Formal analysis, Investigation, Writing – original draft. **Miguel Levy:** Resources, Writing – review & editing. **Hugo E. Hernandez-Figueroa:** Conceptualization, Resources, Writing – review & editing, Supervision, Project administration, Funding acquisition.

#### Data availability

Data is contained within the article.

#### Funding

This work was supported by the National Council for Scientific and Technological Development (CNPq) under Projects No 465757/2014-6 (INCT FOTONICOM) and No 312714/2019-2 (HEHF's Research Productivity Grant); and by the Sao Paulo Research Foundation (FAPESP) under Projects No 2015/24517-8 (Thematic Project "Photonics for Next Generation Internet") and No 2019/13667-0 (Post-Doctoral grant).

## Declaration of competing interest

The authors declare that they have no known competing financial interests or personal relationships that could have appeared to influence the work reported in this paper.

## References

- [1] H. Takeda, S. John, Compact optical one-way waveguide isolators for photonic-band-gap microchips, *Phys. Rev. A* 78 (2) (2008) 023804.
- [2] Y. Shoji, M. Ito, Y. Shirato, T. Mizumoto, MZI optical isolator with Si-wire waveguides by surface-activated direct bonding, *Opt. Express* 20 (16) (2012) 18440–18448.
- [3] Y. Shoji, T. Mizumoto, Silicon waveguide optical isolator with directly bonded magneto-optical garnet, *Appl. Sci.* 9 (3) (2019) 609.
- [4] Q. Du, C. Wang, Y. Zhang, Y. Zhang, T. Fakhrol, W. Zhang, et al., Monolithic on-chip magneto-optical isolator with 3 dB insertion loss and 40 dB isolation ratio, *ACS Photon.* 5 (12) (2018) 5010–5016.
- [5] K. Srinivasan, B.J. Stadler, Magneto-optical materials and designs for integrated TE-and TM-mode planar waveguide isolators: A review, *Opt. Mater. Express* 8 (11) (2018) 3307–3318.
- [6] B.J. Stadler, T. Mizumoto, Integrated magneto-optical materials and isolators: A review, *IEEE Photonics J.* 6 (1) (2013) 1–15.
- [7] P. Pintus, D. Huang, C. Zhang, Y. Shoji, T. Mizumoto, J.E. Bowers, Microring-based optical isolator and circulator with integrated electromagnet for silicon photonics, *J. Lightwave Technol.* 35 (8) (2017) 1429–1437.
- [8] D. Huang, P. Pintus, C. Zhang, Y. Shoji, T. Mizumoto, J.E. Bowers, Electrically driven and thermally tunable integrated optical isolators for silicon photonics, *IEEE J. Sel. Top. Quantum Electron.* 22 (6) (2016) 271–278.
- [9] D. Karki, V. Stenger, A. Pollick, M. Levy, Thin-film magnetless Faraday rotators for compact heterogeneous integrated optical isolators, *J. Appl. Phys.* 121 (23) (2017) 233101.
- [10] M.A. Serrano-Núñez, Y. Shoji, T. Mizumoto, Small magnetless integrated optical isolator using a magnetized cobalt ferrite film, *IEICE Electron. Express* 19 (2) (2022) 20210500.
- [11] M.A. Green, Self-consistent optical parameters of intrinsic silicon at 300 K including temperature coefficients, *Sol. Energy Mater. Sol. Cells* 92 (11) (2008) 1305–1310.
- [12] L.V. Rodríguez-de Marcos, J.I. Larruquert, J.A. Méndez, J.A. Aznárez, Self-consistent optical constants of SiO<sub>2</sub> and Ta<sub>2</sub>O<sub>5</sub> films, *Opt. Mater. Express* 6 (11) (2016) 3622–3637.
- [13] J. Chen, S. Gao, Wavelength-assignable 1310/1550 nm wavelength conversion using completely phase-matched two-pump four-wave mixing in a silicon waveguide, *Opt. Commun.* 356 (2015) 389–394.
- [14] D. Méchin, R. Provo, J. Harvey, C. McKinstrie, 180-nm wavelength conversion based on Bragg scattering in an optical fiber, *Opt. Express* 14 (20) (2006) 8995–8999.
- [15] R. Abbott, V. Fratello, S. Licht, I. Mnushkina, U.S. Patent US 6, 770, 223 B1, Aug. 3, 2004, Article comprising a Faraday rotator that does not require a bias magnet.
- [16] Magneto-optic Faraday rotator garnet crystals, 2020, II-VI Incorporated, Available at <https://app.boxcn.net/shared/static/g7gfmnadkx15t2v4rqk4y87obfylaos.pdf>, Rev. 02.
- [17] Y. Shoji, T. Mizumoto, H. Yokoi, I.-W. Hsieh, R.M. Osgood Jr., Magneto-optical isolator with silicon waveguides fabricated by direct bonding, *Appl. Phys. Lett.* 92 (7) (2008) 071117.
- [18] S. Liu, Y. Shoji, T. Mizumoto, Mode-evolution-based TE mode magneto-optical isolator using asymmetric adiabatic tapered waveguides, *Opt. Express* 29 (15) (2021) 22838–22846.
- [19] A. Barybin, V. Dmitriev, *Modern Electrodynamics and Coupled-Mode Theory: Application to Guided-Wave Optics*, Rinton Press Princeton (NJ), 2002.
- [20] J.D. Joannopoulos, S.G. Johnson, J.N. Winn, R.D. Meade, *Photonic Crystals: molding the Flow of Light*, Princeton University Press, 2011.
- [21] H.A. Haus, W. Huang, Coupled-mode theory, *Proc. IEEE* 79 (10) (1991) 1505–1518.
- [22] G. Portela, V. Dmitriev, T. Oliveira, G. Barros, W. Castro, Graphene-based four-port circulator with an elliptical resonator for THz applications, *J. Comput. Electron.* 20 (6) (2021) 2471–2482.
- [23] V. Dmitriev, G. Portela, L. Martins, Temporal coupled-mode theory of electromagnetic components described by magnetic groups of symmetry, *IEEE Trans. Microw. Theory Tech.* 66 (3) (2017) 1165–1171.